Experimental and numerical investigation on a passive control system for the mitigation of vibrations on SDOF and MDOF Structures: mini Tribological ROCKing Seismic Isolation Device (miniTROCKSISD)

L. Giresini, M.L. Puppio, F. Laccone & M. Froli

Published online: 08 Sep 2021.

Submit your article to this journal

View related articles

View Crossmark data

Taylor & Francis
Taylor & Francis Group

Check for updates

Experimental and numerical investigation on a passive control system for the mitigation of vibrations on SDOF and MDOF Structures: mini Tribological ROCKing Seismic Isolation Device (miniTROCKSISD)

L. Giresini [ID][a], M.L. Puppio[a], F. Laccone [ID][a,b], and M. Froli[a]

[a]Department of Energy, Systems, Territory and Construction Engineering, University of Pisa, Largo Lucio Lazzarino, Pisa, Italy; [b]Institute of Information Science and Technologies 'A. Faedo', National Research Council of Italy, Pisa, Italy

ABSTRACT

This paper illustrates the results of an experimental campaign performed on a scale prototype of a base dissipator called Mini Tribological ROCKing Seismic Isolation Device. This device allows a smooth, controlled and damped rocking by means of frictional layers and viscous elastic springs, which aim at decoupling the frequencies of the superstructure, at dissipating energy during motion and at re-centering the system once the external action vanishes. Four superstructures are tested – a shear type frame, braced and unbraced, a multi-story frame and a SDOF oscillator – with 96 ambient vibration and impulsive tests. An analytical model is illustrated and validated by the experimental tests. The reduction of relative displacement demand is analyzed for all the cases together with the reduction of the acceleration demand, showing positive effects of the base dissipator on the dynamic behavior of all the superstructures.

1. Introduction

Earthquakes are unpredictable phenomena that cause damage of various severities, from a temporary out of service to collapse. To mitigate these effects, seismic control systems can be used modifying the dynamic characteristics of the superstructure. The main outcome is a lowering of frequency and a dissipation of earthquake energy or its transferring through passive, semi-active or active systems. An extensive state-of-the-art of passive control systems is discussed in (Parulekar and Reddy 2009), whereas an overview on active control systems is given in (Soong and Constantinou 1994). The main disadvantage of active or semi-active control systems is their need for external power supply, which can be incompatible with high-intensity earthquakes and is also a unsustainable solution. Among the passive seismic protection systems, the viscous-elastic dampers and friction pendulum isolators are well known and widely used. They belong to the category of energy dissipators (friction dampers and fluid viscous dampers) and base isolators (friction pendulum systems and laminated rubber bearings) (Parulekar and Reddy 2009). The viscous-elastic dampers have the great advantage of being able to simultaneously reduce both accelerations and displacements (Lavan and Dargush 2009). Double and triple friction pendulum isolators imply sliding of the superstructure on two or more curved surfaces that re-center it, thanks to friction and inertia forces (Castaldo and Alfano 2020; Fadi and Constantinou 2010; Fenz and Constantinou 2006). All of them were used both at the base of the structure and at special pivots (center or extremities of bracing systems, beam-to-column joints).

In case of slender structures, such as towers and generic artworks or non-structural objects (steles, statues, busts, showcases, cabinets, etc.), passive devices are generally placed at the base. Some researchers investigated the use of double concave curved surface sliders for marble sculptures (Baggio et al. 2015), statues (Borri and Grazini 2006; De Canio 2012) and busts (Berto, Rocca, and Saetta 2018). In case of multiple art objects exhibited in museums, others proposed base isolated floors consisting in double friction pendulum isolators, which allow protecting more objects with structural optimization and saving of resources (Sorace and Terenzi 2015). The analytical approach for passive vibration control of art objects is presented in (Caliò and Marletta 2003), in which the equations of motion of art objects assumed to be rigid bodies are derived considering the transition from rest, sliding and rocking. All these devices work through a smooth rocking behavior, different from the non-smooth rocking behavior that can also be used as a dynamic control system (Alecci and De Stefano 2018; Casapulla et al. 2019, 2018; De Falco, Giresini, and Sassu 2013; Giresini et al. 2019a, 2019b, 2019c). Critical aspects of the resonance conditions of systems assumed to be rigid bodies (Casapulla 2015; Casapulla and Maione 2017) and stochastic approaches (Lallemant, Kiremidjian, and Burton 2015; Stochino, Attoli, and Concu 2020) could also be considered.

A special class of passive control systems couples the phenomenon of energy dissipation with the modification of the structural dynamic properties. In particular, recently a seismic isolator, called Tribological ROCKing Seismic ISolation Device (TROCKSISD) has been conceived by M. Froli. TROCKSISD is an articulated device that protects the superstructure from shocks and vibrations induced by dynamic actions. The conceptual idea of this device, whose design follows the performance based seismic design criteria, is extensively illustrated in (Froli, Giresini, and Laccone 2019a). This isolator is suitable to protect from earthquakes or base vibrations slender structures, such as towers or art objects of small dimensions.

The device is composed of two main components in contact through spherical surfaces and a set of elastic dampers (Figure 1). There are two sources of energy dissipation: the frictional surfaces, whose effect can be tuned by the precompression of peripheral springs, and the viscous dampers mounted in parallel with springs (Figure 1a). The springs that are co-axial to the dampers dissipate energy and re-center the superstructure.

This paper illustrates the results of an experimental campaign performed on a scale prototype of TROCKSISD, called miniTROCKSISD (MT). The full-scale prototype is shown in Figure 2a as a seismic device conceived for a glass-steel hybrid slender structure, whereas Figure 2b indicates the experimental setup that will be considered for its future testing. The scale of the experimental prototype for the full-scale specimen is 1:5. This campaign has the aim of validating the theoretical approach proposed in (Froli, Giresini, and Laccone 2019a, 2019b) for this class of passive control systems. Section 2 illustrates
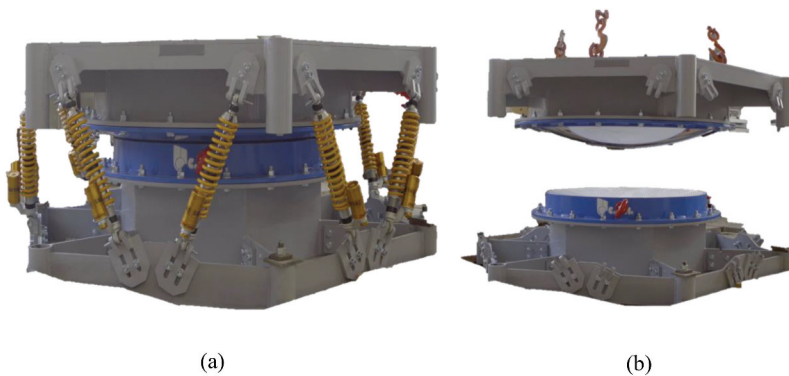

(a)   (b)

Figure 1. (a) TROCKSISD prototype with (b) the view of spherical frictional surfaces.
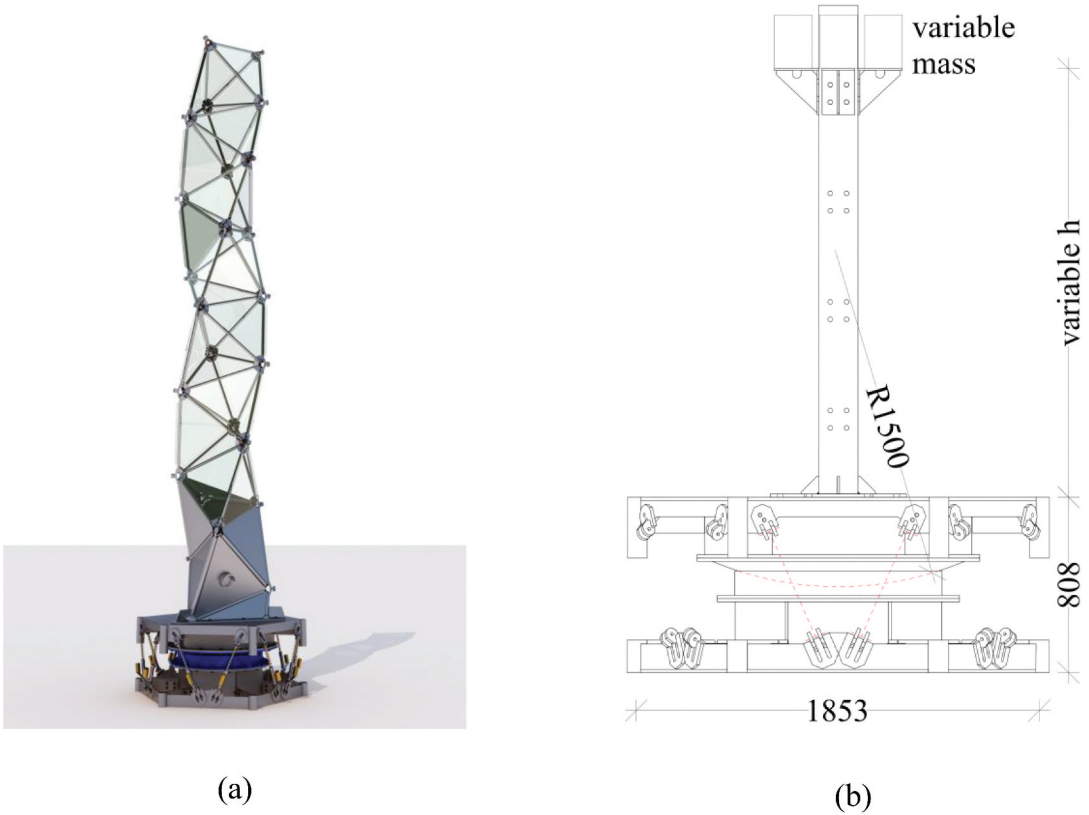
Figure 2. (a) TROCKSISD applied at the base of a slender structure (b) supposed experimental setup (units in mm).

the experimental tests performed on four superstructures mounted on MT. Section 3 discusses the experimental outcomes comparing the dynamic behavior of the non-isolated structure with the structure isolated through MT. In Section 4 an analytical model of the tested configurations is proposed, and numerical tests are carried out to validate it by cross-checking the experimental results in Section 5.

2. Mini Tribological ROCKing Seismic ISolation Device – Mini TROCKSISD

2.1. Description of the specimens

The device, shown in Figure 1, whose planar dimension is about 2×2 m^2, is studied in this paper through a scaled device (Figure 3). The spherical configuration of the interface (Figure 1b) is modified into a cylindrical shape to simplify the smooth rocking, switching it from 3D motion to an in-plane motion.

The main components of MT (Figure 3) and their functions are summarized in the following.

- The superstructure (Figure 4a) represents the object to protect from vibrations induced by earthquakes or, in general, by dynamic actions. It is composed of multi-hole bars to connect with masses for realizing multiple configurations.
- The convex cylindrical plate, centered in O (Figure 4b), is the main component where smooth rocking occurs. Through its surface, energy is dissipated by friction on an ETFE sheet, which, in turn, is connected to the concave plate underneath it.
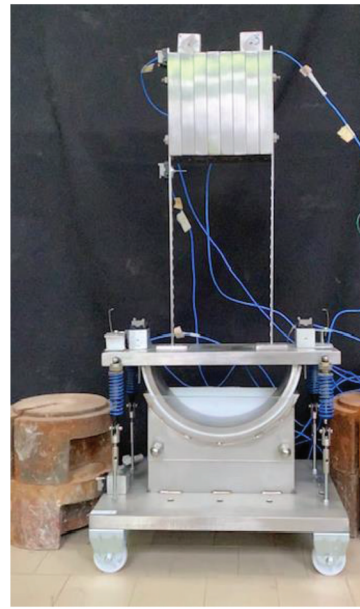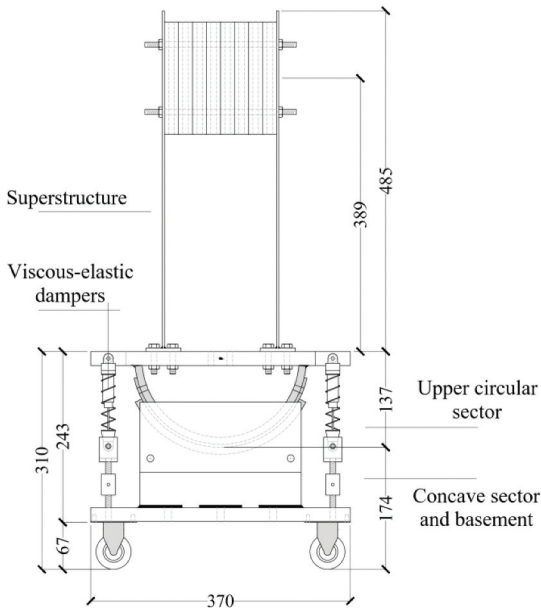
Figure 3. Overall view of MT with (a) indication of the main components (units in mm); (b) device assembled in the laboratory.
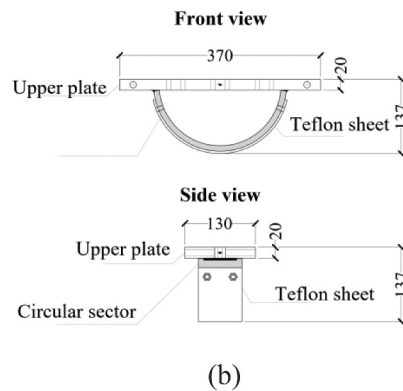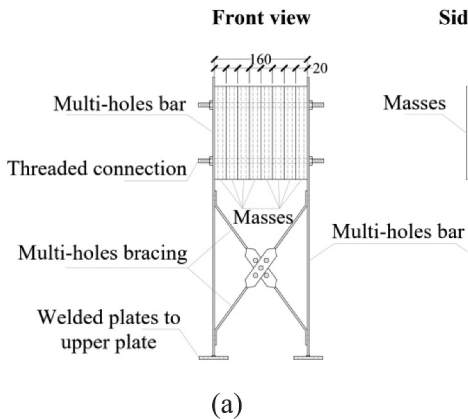
Figure 4. (a) Superstructure and (b) upper circular sector of MT (units in mm).

- The concave cylindrical plate (Figure 5) is made of a curved steel plate installed on a ribbed support. The basement is a 20 mm thick base plate of dimensions 370 mm x 278 mm and has 6 threaded holes to allow the placement of bracket connections, which accommodate the bottom part of the viscous elastic devices. The basement has four wheels. Two lateral restraints prevent possible out-of-plane mechanisms that can occur during the test.
- Pairs of viscous-elastic dampers connect the upper plate of the convex sector and the plate of the basement. These devices are used to add stiffness (k), damping (c), and re-centering capacity to the system.
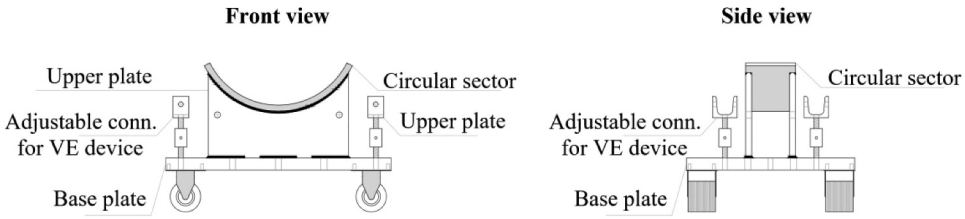
Figure 5. Concave sector and basement of MT (units in mm).

The specimen has a total height of 727 mm, including a superstructure that spans for 485 mm. The total width and depth of the device are, respectively, 370 mm and 278 mm. Concerning the materials, common steel is used for all the components, while the sliding surfaces are made of stainless steel and anodized aluminum.

2.2. Experimental Test Setup of MT

MT is tested to understand its capabilities in isolating a generic superstructure from vibrations and in dissipating energy provided by earthquake-type actions. From a mechanical point of view, the MT dynamic response strongly depends on the mass and stiffness of the superstructure, on the stiffness and damping of the lateral dissipative devices, and on the friction developed at the interface of the two cylindrical plates (§ 2.1).

Typical configurations of the superstructure, which are frequently found in real cases, are considered. They vary in terms of mass and bars disposal and can be associated with Single Degree Of Freedom (SDOF) or Multiple Degrees Of Freedom (MDOF) models, as specified below. In order to evaluate the effect of the isolation provided by the MT on the dynamic response of the system, each scheme is preliminarily tested in a non-isolated setting, namely rigidly connecting the superstructures to the ground. In particular, four schemes are considered (Fig. 6); each one is labeled with an acronym composed by the number of vertical elements (2P or 1P, where P stands for "pillars"), the number of masses (4 M or 8 M) and the system to counteracts horizontal actions (bracing system, X, shear-type, T and cantilever, V). Each mass is of 1.75 kg. The first and the second schematics count eight masses; the first one is braced. The third and the fourth schematics have a total of four masses; the third one is a shear-type frame and the last one a cantilever with a single vertical element, similar to the traditional SDOF oscillator.
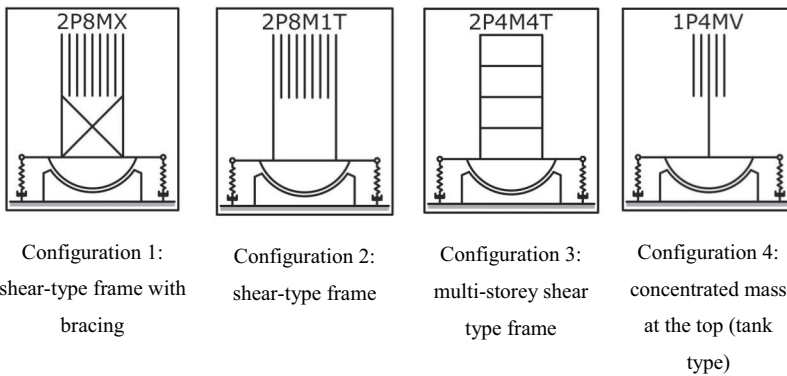

Figure 6. The four configurations tested in the experimental tests.

Each schematic corresponds to simplified SDOF and MDOF systems. In particular, schemes C_1, C_2 and C_4 are 2DOF systems: the degrees of freedom are the translation of the superstructure in the horizontal direction x and the rotation α of the base around the pivoting point (Figure 7). Scheme C_3 is a 5DOF system: four horizontal translations of each story x_i and the rotation α of the base around the pivoting point.

As already pointed out, two conditions are investigated: one with the isolation device (defined in the following "with MT") and another one in which the superstructure is not isolated and fixed at the base ("without MT"). Moreover, two dynamic tests are performed to dynamically identify the structure: an ambient vibration test and an impulsive test, where the force has been provided by a calibrated impact hammer. Two ambient vibration tests are performed for each schematic and for each condition for a sampling time of 7 minutes, for a total number of 16 tests. In addition, 10 impulsive tests for each configuration and for non-isolated and isolated system, with an instrumented hammer, have been carried out for each schematic and for each condition, for a total number of 80 tests. The instrument used here is an impact hammer PCB Piezotronics Model 086D20, equipped with a transducer tip of average hardness 084A62. The outputs of the 96 tests are measured in terms of accelerations given by accelerometers, disposed as shown in Fig. 8.

2.3. Experimental Test Setup on Single Components

Before testing the assembled prototype, several tests on individual components are performed to identify their mechanical characteristics. This step is necessary to acquire reliable mechanical parameters for the phase of cross validation of the analytical model presented in Section 4. The individual components constitute the viscous-elastic dampers and the interface between concave and convex sectors – described in § 2.1. More in detail, three groups of tests are carried out. The first group investigates the stiffness of the springs, which should be able to re-center the superstructure during the smooth rocking. The second group investigates the dampers, which aim at dissipating energy over motion. The third group aims at the characterization of the frictional moment occurring along a concave cylindrical surface.

2.3.1. Tests on Springs
The springs are part of the viscous-elastic dampers and are tested separately from the damper. In the test setup, each spring is located between two rigid plates; the upper plate is loaded by progressively adding masses of about 300 g each causing the spring compression (Fig. 10a). The axial load is applied through five subsequent steps by increasing the masses on the upper plate. The data are measured by
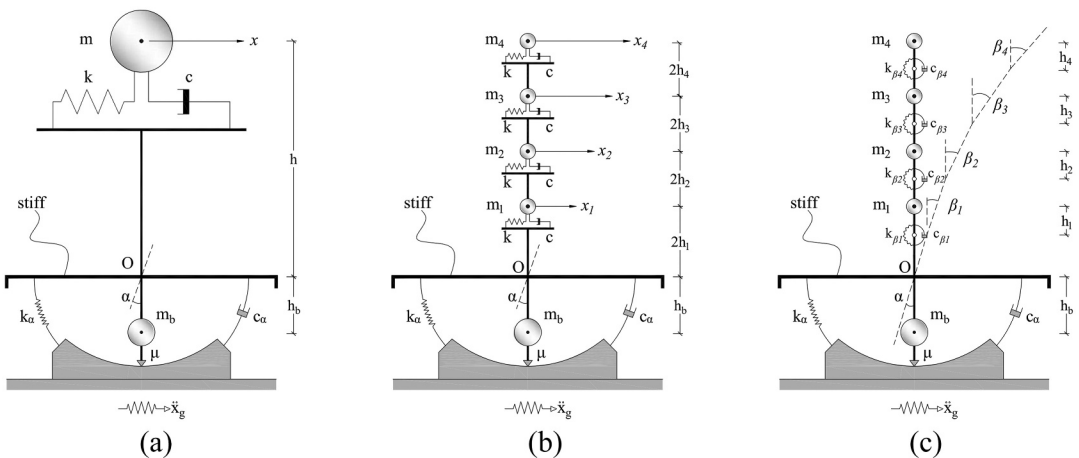

Figure 7. Single Degree of Freedom and Multiple Degrees of Freedom systems representative of the four configurations tested.

Configuration 1: shear-type frame with bracing

Configuration 2: shear-type frame

Configuration 3: multi-storey shear type frame

Configuration 4: concentrated mass at the top (SDOF oscillator)
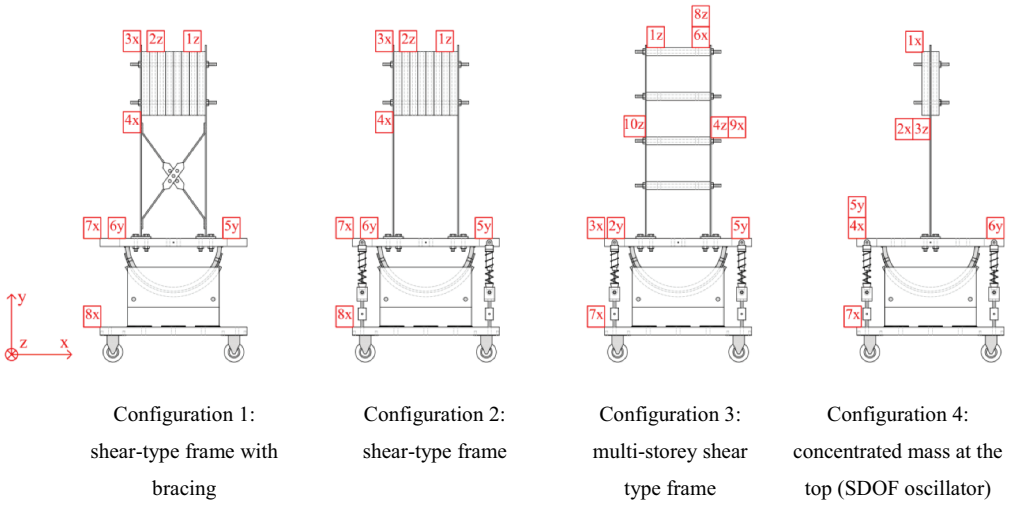
Figure 8. Disposition of accelerometers in the tested configurations.
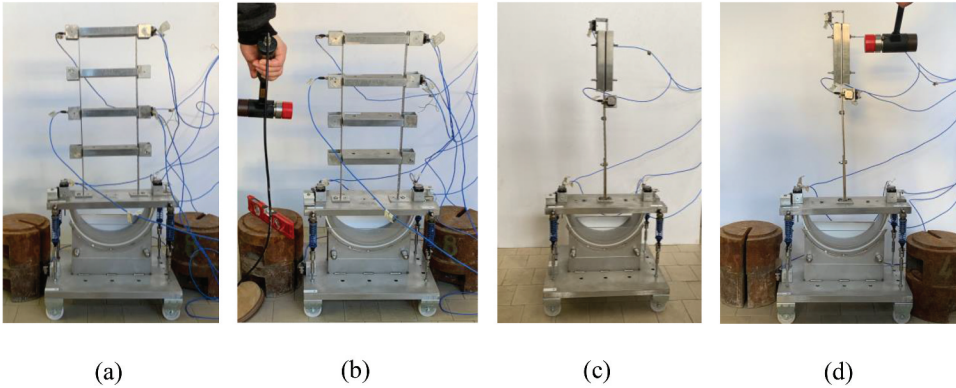

(a) (b) (c) (d)

Figure 9. (a, b) Configuration C_3 and (c, d) C_4 tested with impulsive force applied through a calibrated hammer.
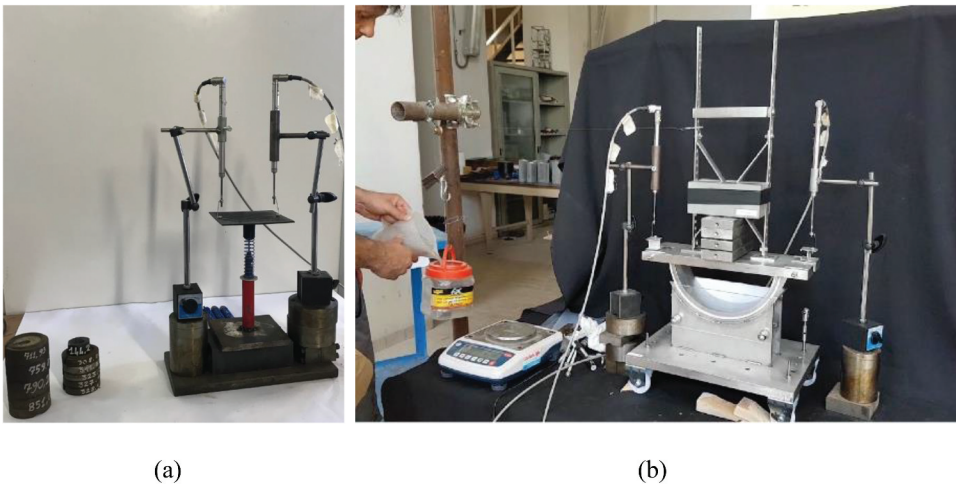

(a) (b)

Figure 10. Characterization of (a) spring stiffness and (b) frictional coefficient.

means of a couple of linear variable displacement transducers (LVDT), whose average displacement value is adopted as system response. The outputs are acquired with a time interval of 2 seconds. Each data set contains approximately 100 values of displacement. The stiffness of the springs is computed by the slope of the force-displacement curve as discussed in § 3.1.

2.3.2. Tests on Dampers

The test setup of the dampers is similar to the springs. The damper is compressed between two rigid plates by the masses, which are gradually added to an upper rigid plate. Four subsequent loads are applied: 0.93, 1.25, 1.57, 2.22 daN. Once the compression of the damper attains a stable value, the load is removed and the return velocity is measured to get the equivalent viscous coefficient. For each of the four dampers, each test is repeated twice.

2.3.3. Tests on the Frictional Cylindrical Surface

A fundamental mechanical parameter that influences the smooth rocking is the friction at the interface between the convex sector and the concave sector. For this reason, a static test is performed to assess the static friction coefficient. In particular, the test consists in applying an increasing load, i.e. pouring sand manually into a bucket, until it causes the device to rotate (Fig. 10b). The force necessary to trigger the mechanism is registered, so the frictional coefficient can be calculated by means of the Coulomb's model. The test is performed twice for each direction of rotation.

3. Results and Discussion of the Experimental Tests

This section contains a summary of the most important experimental results and discusses them in terms of dynamic response and effectiveness of the MT device, compared with the condition without base isolation.

3.1. Mechanical Features of the Single Components

The tests on **springs** described in § 2.3.1 allow obtaining the force-displacement relationships displayed in Fig. 11. The values of spring stiffness k that are obtained from the test range from 0.55 to 0.70 daN/cm, with a mean value of 0.67 daN/cm.

Concerning the tests on the **dampers**, the viscous constant is calculated by adopting the Kelvin's solid model. In particular, given $s(t_1)$ the maximum displacement measured by the LVDTs at time t_1, F_0 the applied force, the viscous constant η can be derived from the following expression.

$$s(t_1) = \frac{F_0}{k} \left(1 - e^{-\frac{t_1 k}{\eta}} \right) \tag{1}$$

Figure 12 displays the force-velocity samples of the four assembled dampers with their interpolating curves. The results highlight the dependency of the viscous constant on the applied load. The viscous constant ranges from 1.56 daNs/cm to 3.03 daNs/cm.

For what concerns the tests on the **frictional surface**, as stated in § 2.3.3, a horizontal load is manually applied by pouring sand into a bucket. This causes the rotation of the device in counter-clockwise direction (Fig. 13a). The moment of the applied load Fb is balanced by the frictional moment M_μ as follows:

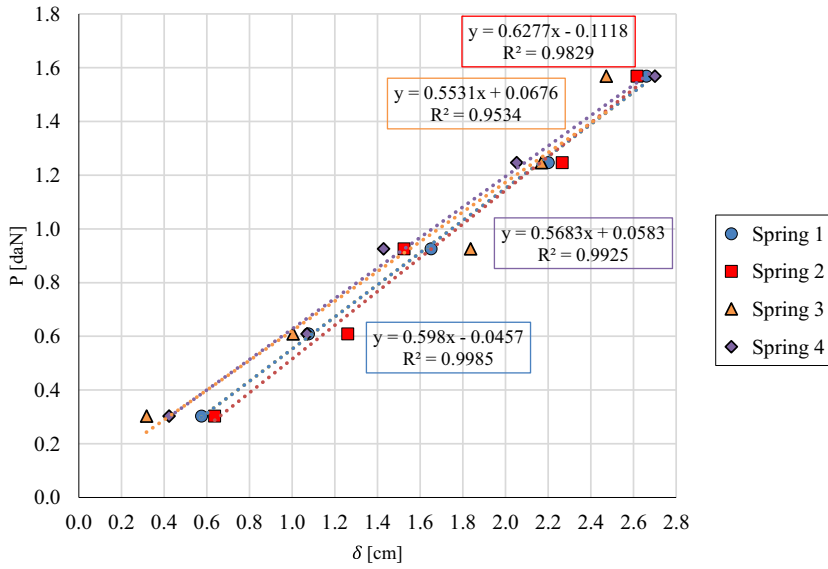$$F \cdot b = M_\mu = \mu_s N \cdot R \tag{2}$$

Figure 11. Force-displacement relationships of the springs used in MT.
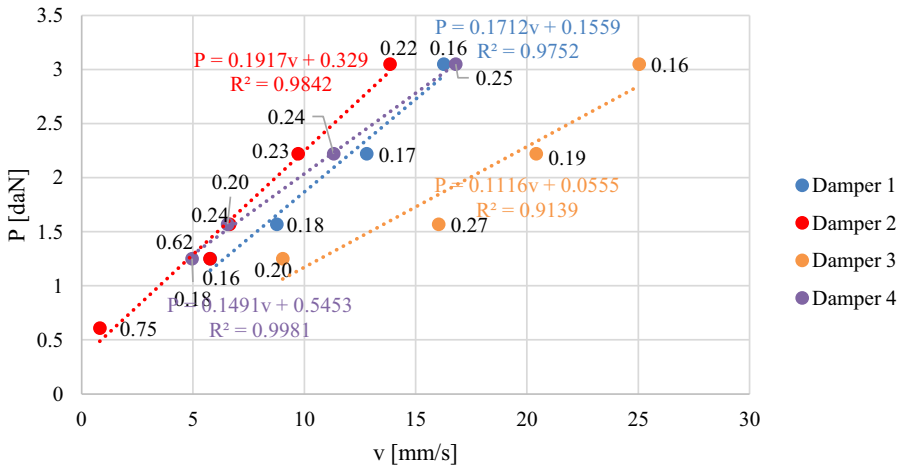

Figure 12. Force-velocity relationships of the assembled dampers used in MT.

Where b is the lever arm of the force F and R is the radius of the cylindrical surface (Fig. 13a). The test is performed by applying the force F in both horizontal directions $\mp x$. From Equation (2), it is immediate to obtain the value of the static friction coefficient μ_s. The results show that, test after test, the coefficient slightly changes and its mean value, obtained neglecting the maximum and minimum values, is about 0.22 (Fig. 13b).
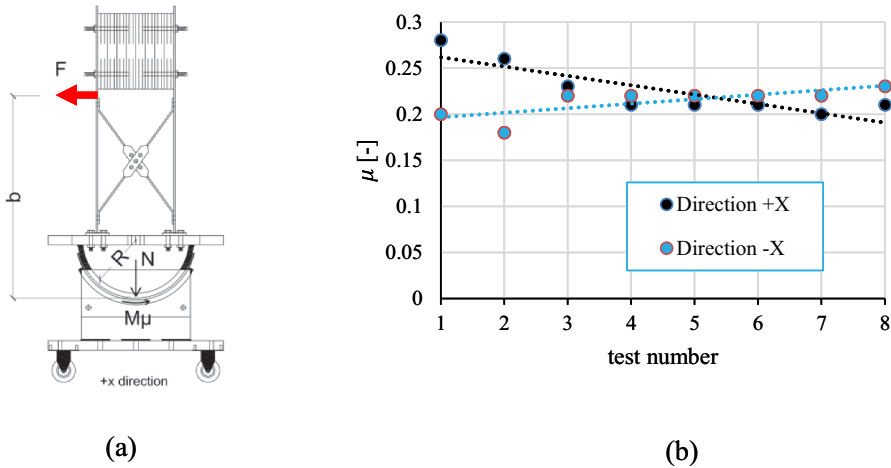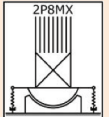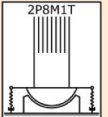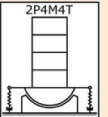
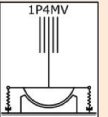(a)   (b)

Figure 13. Determination of static friction coefficient at the cylindrical interface: (a) experimental set-up (see also Fig. 10b) and (b) results in terms of static friction coefficient.

3.2. Comparison between Isolated and Non-isolated Superstructure

This paragraph discusses the comparison between the superstructure isolated by MT and super-structure fixed at its base. The ambient vibration tests give the dominant frequencies of the four configurations in x direction (in-plane) and in z direction (out-of-plane). The results highlight that the isolated superstructure is characterized by eigenfrequencies lower than those of the non-isolated superstructure, as expected (first row of Table 1). This beneficial effect is visible, in particular for configuration C_4, in which a reduction by 15% is obtained. Other than for C_4, the maximum reduction of eigenfrequency is obtained for C_3, with a difference by about 11%. During the ambient vibration testing, the configuration of MT is stuck, that is, the static frictional coefficient is not attained. Therefore, MT is mechanically characterized neglecting such a non-linear aspect and that is why the increase of eigenfrequencies is not so relevant. Nevertheless, it is worth observing that this effect is associated with a reduction of spectral acceleration for the isolated structure. To investigate this aspect, one can examine the acceleration time-histories for both scenarios of the four configurations. A comparison of the results obtained by applying an impulsive force through a calibrated hammer are reported in Fig. 14. These acceleration time

Table 1. Dominant experimental eigenfrequencies obtained from ambient vibration tests on the superstructure with MT and on the non-isolated superstructure (without MT).

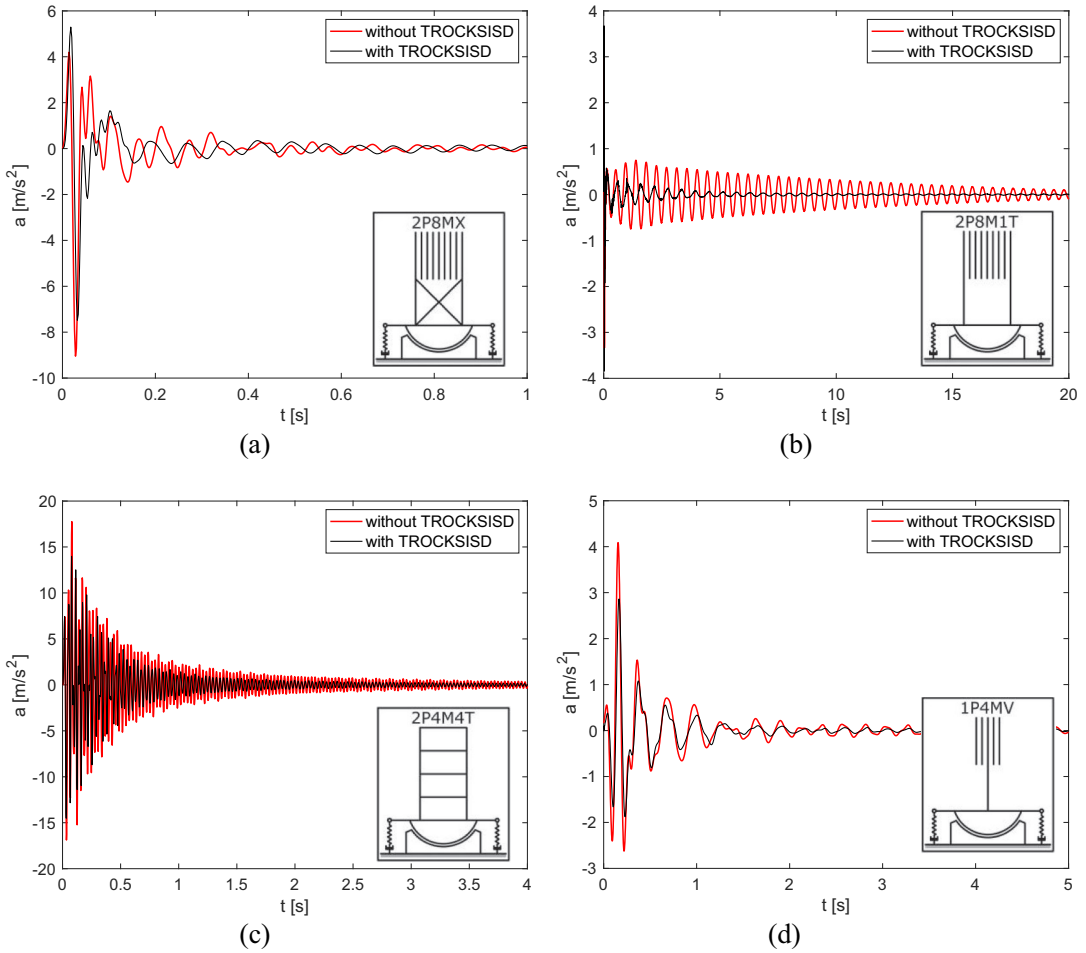|	C_1 2P8MX			C_2 2P8M1T			C_3 2P4M4T			C_4 1P4MV		
	MT ✗	MT ✓	Δw/o-With (%)	MT ✗	MT ✓	Δw/o-With (%)	MT ✗	MT ✓	Δw/o-With (%)	MT ✗	MT ✓	Δw/o-With (%)
f_{exp} [Hz]	16.8	15.6	-6.9%	2.4	2.3	-7.4%	9.6	8.6	-10.6%	2.6	2.2	-15.1%
f_{num} [Hz]	16.5	16.2	-1.5%	2.6	2.4	-8.0%	10.3	8.6	-16.1%	2.6	2.4	-9.5%
$\Delta_{exp-num}$ (%)	-1.8%	3.8%		7.8%	7.1%		7.3%	0.7%		1.5%	8.2%	

Figure 14. Comparisons between acceleration time histories of isolated and non-isolated superstructure: (a) C_1, (b) C_2, (c) C_3, (d) C_4.

histories are selected from the 80 tests considering similar amplitudes of impulsive inputs. As an example, the first configuration has an acceleration peak of 9 m/s² which reduces to 7.6 m/s² in case of isolation (Fig. 14a). The strongest reduction is mostly visible for the shear type frames, both unbraced and braced, at a larger extent for the unbraced configuration (Fig. 14a-b).

Considering the maximum peaks after the application of the impulsive force, the reduction from the non-isolated to the isolated structure is by 17%, 13%, 14% and 30% respectively for configuration C_1, C_2, C_3 and C_4. The velocity and displacement time histories are obtained by integration of the acceleration time history of each configuration. The displacement TH is displayed in absolute terms for the sake of comparison between the two configurations. The contemporary reduction of acceleration response and increase in displacement demand are shown for the braced frame in Fig. 15: the reduction of maximum displacement is by 56%. Instead, for the cantilever SDOF oscillator (C_4), the same reduction is by 46%, but the displacement values are one order of magnitude higher than those of C_2 (Fig. 16). Therefore, even if the reduction of eigenfrequency of C_4 is only half of C_2 (Table 1), the reduction of maximum displacement is still relevant.
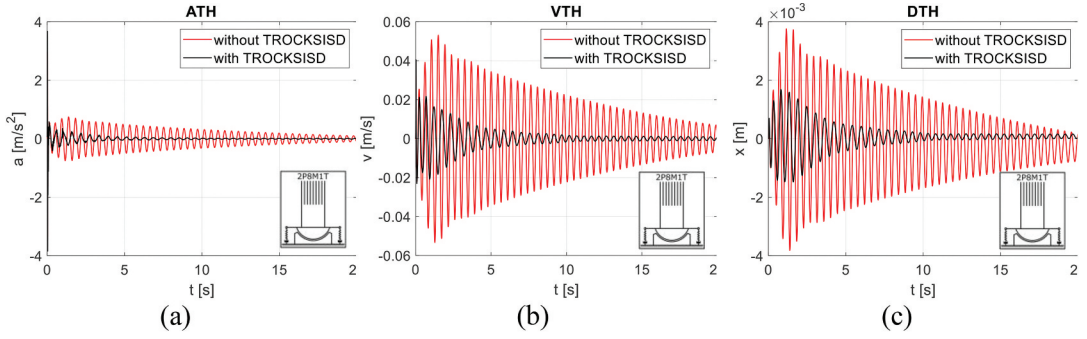
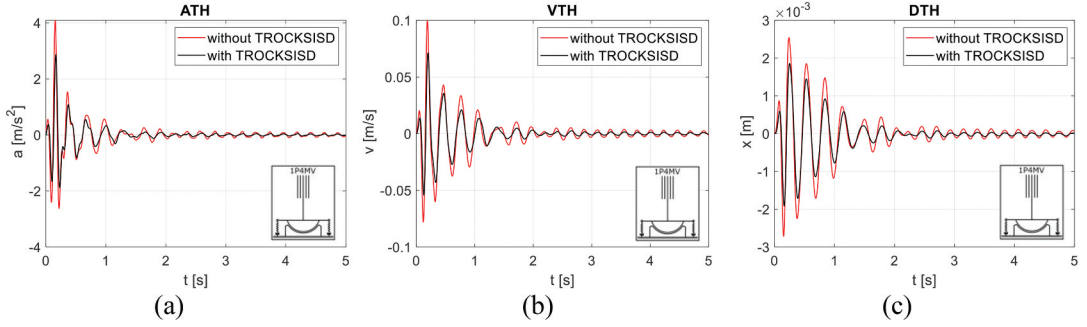**Figure 15.** Braced frame structure (C_2): (a) acceleration, (b) velocity, (c) displacement time histories.

Figure 16. SDOF oscillator (C_4): (a) acceleration, (b) velocity, (c) displacement time histories.

4. Analytical Model and Numerical Analyses

4.1. Equations of Motion

The analytical model here introduced simulates the dynamic behavior of the four superstructures with and without MT. The results predicted by the analytical model are cross-checked with the experimental results. Two different analytical models can be considered, one for the non-isolated superstructure and another for the superstructure isolated by MT.

As for the non-isolated superstructure of mass m and stiffness k, the SDOF systems (configurations 1, 2 and 4 of Fig. 6) cyclic frequency is obtained with the well-known expression $f = 2\pi\sqrt{m/k}$. The eigenfrequencies of C_3 can be easily obtained by solving the equations of motion in free vibration regime for MDOF systems.

When the isolated superstructure is considered, an additional degree of freedom, which is the rigid rotation α of the base isolator, has to be taken into account. For the 2DOF system (rotation α and horizontal displacement x, Figure 7a), the equations of motion are as follows (Froli, Giresini, and Laccone 2019a):

$$\begin{cases} m\ddot{x} + c\dot{x} - ch + kx\dot{\alpha} - kh\alpha = -m\ddot{x}_g \\ I_b\ddot{\alpha} + (c_\alpha + ch^2)\dot{\alpha} + (k_\alpha + kh^2)\alpha - ch\dot{x} - khx + M_\mu = -m_b h_b \ddot{x}_g \end{cases} \tag{3}$$

Where c is the equivalent viscous coefficient of the superstructure, h the distance between center of rotation O and center of mass of the superstructure, x_g the seismic acceleration time history. Moreover, I_b is the inertia moment of MT, c_α and k_α respectively the rotational viscous coefficient and stiffness, h_b the distance between the center of rotation O and the center of mass of MT. M_μ stands for the frictional moment developed at the interlayer between the two cylindrical surfaces.

The modal analysis is performed by solving the eigenvalues problem associated to the following system:

$$\begin{cases} m\ddot{x} + c\dot{x} - ch\dot{\alpha} + kx - kh\alpha = 0 \\ I_b\ddot{\alpha} + (c_\alpha + ch^2)\dot{\alpha} + (k_\alpha + kh^2)\alpha - ch\dot{x} - khx = 0 \end{cases} \quad (4)$$

obtained by neglecting the external excitation term and the frictional moment.

As for configuration C_3, one needs to write the equations of motion of a five degrees of freedom system (shown in Figure 7) in terms of translational degrees of freedom:

$$\begin{cases} m_4\ddot{x}_4 + k_4 \cdot (x_4 - x_3) = -m_4\ddot{x}_g \\ m_3\ddot{x}_3 + k_3 \cdot (x_3 - x_2) - k_4 \cdot (x_4 - x_3) = -m_3\ddot{x}_g \\ m_2\ddot{x}_2 + k_2 \cdot (x_2 - x_1) - k_3 \cdot (x_3 - x_2) = -m_2\ddot{x}_g \\ m_1\ddot{x}_1 + k_1 \cdot (x_1 - 2h_1\alpha) - k_2 \cdot (x_2 - x_1) = -m_1\ddot{x}_g \\ I_b\ddot{\alpha} + c_\alpha\dot{\alpha} + k_\alpha\alpha - 2k_1 \cdot h_1 \cdot (x_1 - 2h_1\alpha) + M_\mu = -m_b h_b \ddot{x}_g \end{cases} \quad (5)$$

or, in terms of rotational degrees of freedom:

$$\begin{cases} Im_4\ddot{\beta}_4 + c_{\beta 1}\left(\dot{\beta}_4 - \dot{\beta}_3\right) + k_{\beta 4}(\beta_4 - \beta_3) = -m_4\ddot{x}_g h_4 \\ Im_3\ddot{\beta}_3 + c_{\beta 3}\left(\dot{\beta}_3 - \dot{\beta}_2\right) - c_{\beta 4}\left(\dot{\beta}_4 - \dot{\beta}_3\right) + k_{\beta 3}(\beta_3 - \beta_2) - k_{\beta 4}(\beta_4 - \beta_3) = -m_3\ddot{x}_g h_3 \\ Im_2\ddot{\beta}_2 + c_{\beta 2}\left(\dot{\beta}_2 - \dot{\beta}_1\right) - c_{\beta 3}\left(\dot{\beta}_3 - \dot{\beta}_2\right) + k_{\beta 2}(\beta_2 - \beta_1) - k_{\beta 3}(\beta_3 - \beta_2) = -m_2\ddot{x}_g h_2 \\ Im_1\ddot{\beta}_1 + c_{\beta 1}\left(\dot{\beta}_1 - \dot{\alpha}\right) - c_{\beta 2}\left(\dot{\beta}_2 - \dot{\beta}_1\right) + k_{\beta 1}(\beta_1 - \alpha) - k_{\beta 2}(\beta_2 - \beta_1) = -m_1\ddot{x}_g h_1 \\ I_b\ddot{\alpha} + c_\alpha\dot{\alpha} + c_{\beta 1}\left(\dot{\beta}_1 - \dot{\alpha}\right) - k_{\beta 1}(\beta_1 - \alpha) + M_\mu = -m_b h_b \ddot{x}_g \end{cases} \quad (6)$$

where I_{mi} is the inertia moment of the i-th mass, $c_{\beta i}$ and $k_{\beta i}$ respectively the rotational damping coefficient and the rotational stiffness associated to the i-th mass. The five Lagrangian parameters are the rotation β_i of the i-th mass and the base rotation α. Finally, the distances from the masses h_i are reported in Figure 7.

These distances are constant and equal to h for the case under examination. Moreover, to validate the experimental results with forced vibration tests with calibrated hammer, $x_g = 0$ and only the third degree of freedom (Figure 9b) has been forced. For this, $-m_3 x_g = F$ where F is the impulsive force exerted by the hammer. Again, to obtain the modal properties, the eigenvalues problem with null friction moment and external excitation is solved (Table 2).

The complete equations of motion are numerically solved via a MATLAB code (MATLAB 2018) specifically written considering both free vibration and impulsive forces with the aim of comparing numerical results with experimental tests.

4.2. Validation of the Analytical Model

The responses predicted by the numerically solved analytical model are here compared to experimental results to verify its reliability. The third row of Table 1 Δ (%) lists the percentage differences between the eigenfrequencies obtained with the numerical model and those given by the corresponding experimental tests. The considered scenario is that of the isolated structure, that is when the structure is equipped with MT. The results in terms of eigenfrequencies are in excellent agreement for configurations C_1 and C_3 (differences by less than 5%) and in very good agreement for C_2 and C_4, with a maximum difference by about 8% (Table 1).

As for the comparison between displacement time-histories (TH), Fig. 17 displays experimental and numerical outputs of the four configurations. The numerical TH are calculated through integration of the acceleration TH provided by the accelerometer. The calculation is performed according to
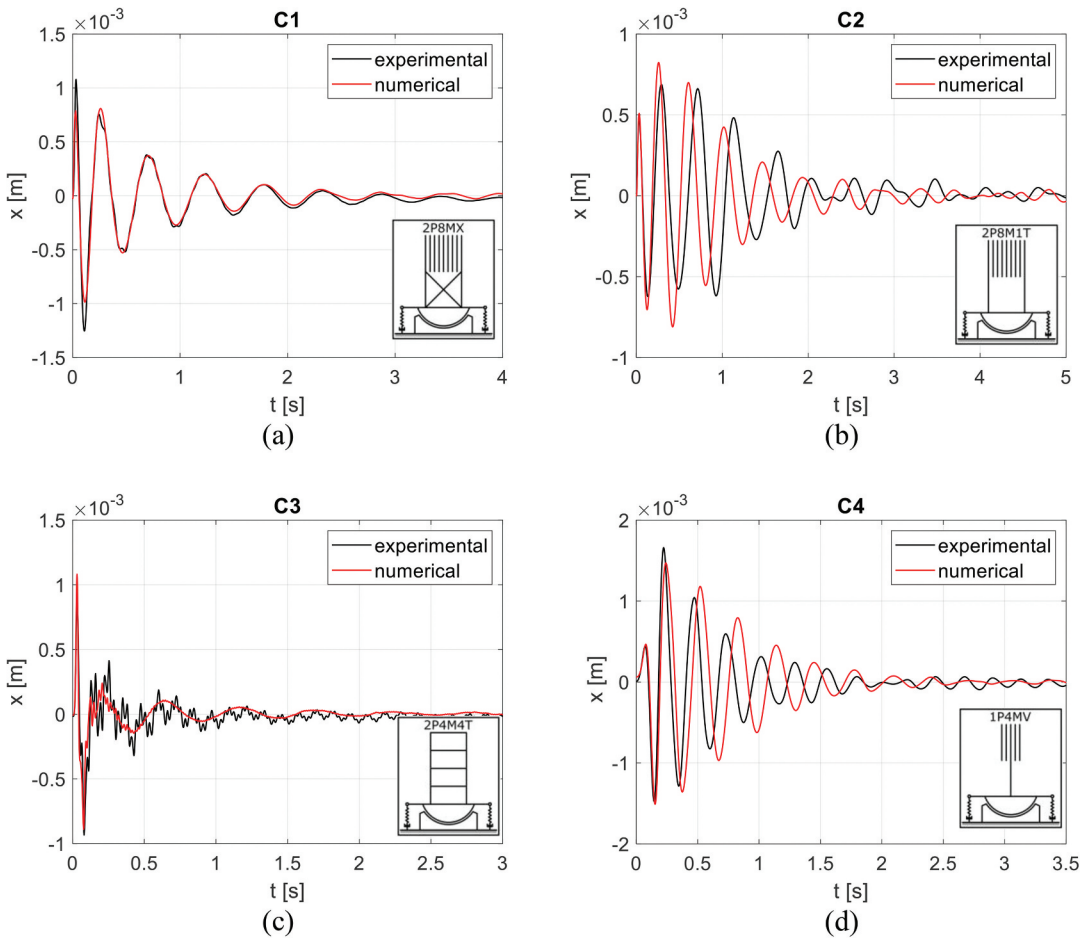
Figure 17. Comparisons between experimental and numerical displacement time-histories for the four configurations: (a) C_1, (b) C_2, (c) C_3, (d) C_4.

the method illustrated in (Giresini, Sassu, and Sorrentino 2018). The experimental outputs have been filtered in the range of frequency 2–50 Hz and compared with the TH predicted by the analytical model solving Eqs. (3) and (5).

It can be observed that the results are in good agreement for C_1 (shear-type frame with bracing): even though the first peak is underestimated by the numerical analysis, the following peaks are perfectly the same (Fig. 17a). In this case, the lowest value of viscous-elastic damping obtained from experimental tests on the single components has been assumed (§ 3.1). Instead, for C_2 (shear-type frame without bracing) the experimental trend is correctly reproduced for the first peaks (Fig. 17b). For configuration C_3, the peaks are correctly reproduced even though there are some high frequencies in the experimental output. For configuration C_4, the numerical curve underestimates the response only for the second positive peak, and for the following cycles, there is a delay of the numerical response.

4.3. Effectiveness of miniTROCKSISD on Different Superstructures

This section discusses the beneficial effects provided by the base dissipator in terms of reduction of acceleration demands. First, the dynamic properties of the non-isolated and isolated superstructures are considered. The frequency of the isolated superstructure f_{MT}, normalized to that of the non-isolated structure f_s, gives the dimensionless frequency plotted in Fig. 18 against the normalized stiffness $k_s/k_{s,MT}$, where k_s is the stiffness of each superstructure (in F/L) and $k_{s,MT}$ is the stiffness of the springs belonging to MT. Given that $k_{s,MT} = 600N/m$, for all the configurations, although the normalized stiffness spans between 1 and 250, the reduction of eigenfrequency is quite similar, since f_{MT}/f_S spans from 0.85 to 0.93. However, C_1, C_2 and C_3 have a closer behavior, as expected since the fourth configuration is remarkably different from the others. More in detail, C_1 and C_2 only differ from the presence of bracing, which, nevertheless, does not change the modification of the behavior with the base isolator ($\frac{f_{MT}}{f_S} = 0.93$ for both). The similarity of such a reduction is a favorable outcome, since for very different superstructures the change of vibration frequency is unremarkable.

Secondly, the reduction of acceleration demand is calculated for each configuration as follows. In a variable range of time t equal to 1 s, 2 s or 5 s, the mean values of acceleration peaks $\bar{a}_j^i$ are considered for each applied impulsive load j (Fig. 19a), where i is the configuration label (from C_1 to C_4). The term $\bar{a}_{j,I}^i$ is the input acceleration of the jth impulse. The mean of all the impulsive loads for each configuration is $\bar{a}^i$ and $\bar{a}_{MT}^i$ respectively for the non-isolated and the isolated structure. These values are normalized to the corresponding mean values of the inputs:

$$R_a = \frac{\bar{a}^i}{\bar{a}_I^i}; R_{a_{MT}} = \frac{\bar{a}_{MT}^i}{\bar{a}_{I,MT}^i} \tag{7}$$

Finally, the percentage of reduction of normalized acceleration peaks reads:

$$\Delta a = \frac{R_a - R_{a_{MT}}}{R_a} \cdot 100 \tag{8}$$

An example of results for configuration C2 is reported in Fig. 20b, where the empty dots represent the single R_{aj} for each impulsive test considering different time ranges.

All the results are reported in Fig. 20, where the abscissa in the logarithmic scale for the sake of better readability: if one considers the period of 5 seconds, the results are more scattered, whereas for periods of 1 second and 2 seconds the variation of acceleration is quite similar except for C_1. For C_1, percentage of
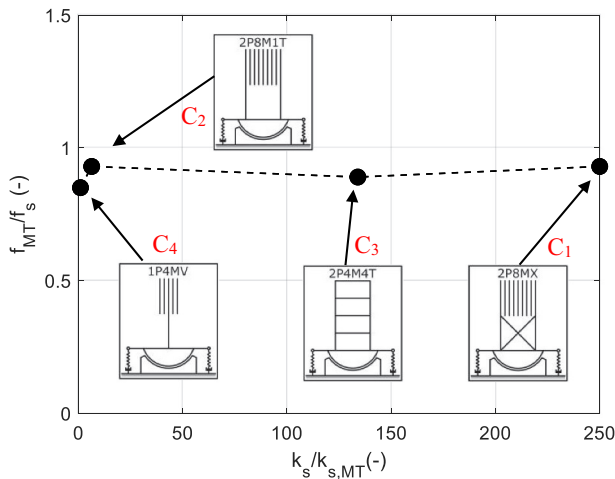

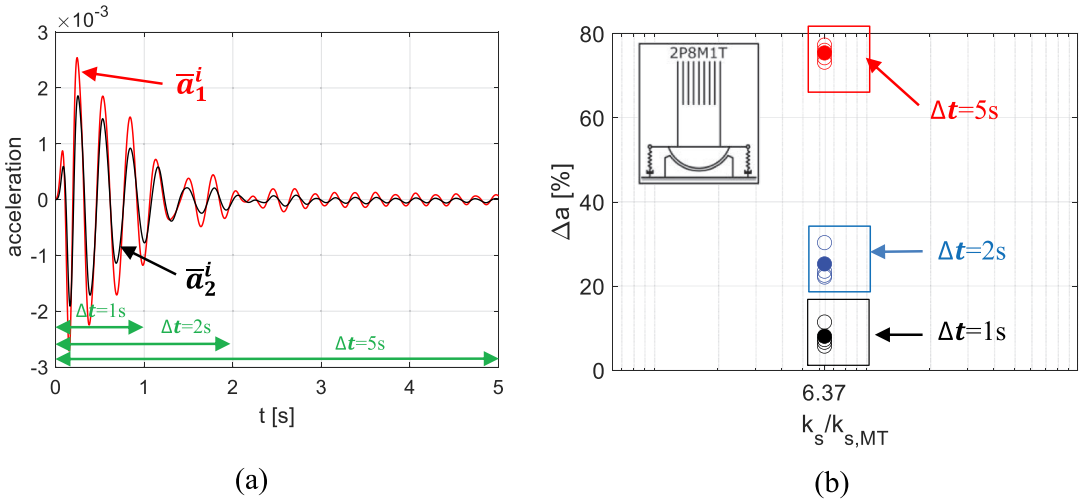**Figure 18.** Normalized frequency versus normalized stiffness of the isolated structures.

Figure 19. Methodology for identifying the variation of acceleration from isolated and non-isolated superstructure: (a) selection of two acceleration time histories for configuration C_i and two hammer tests, considering different time ranges; (b) average values for each hammer test and for different time ranges for C_2.
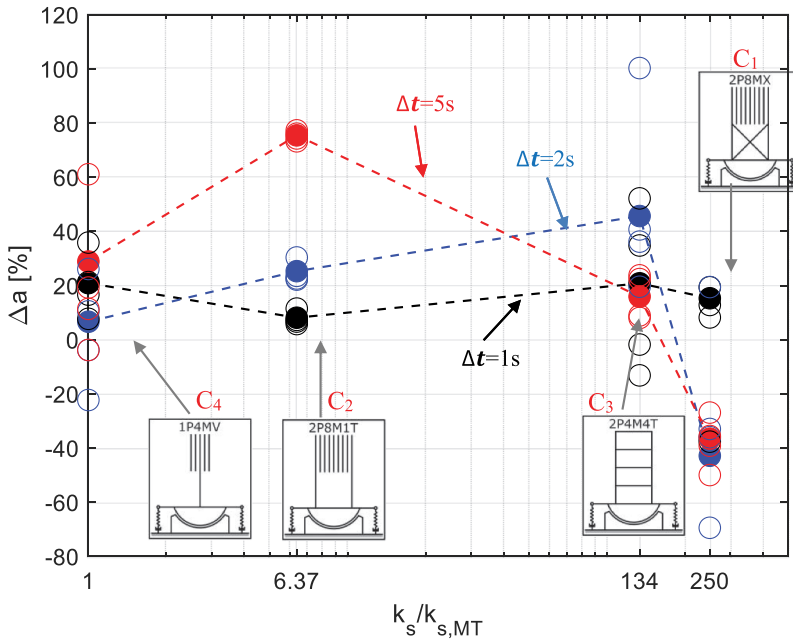

Figure 20. Reduction of acceleration demand in the isolated structures.

Table 2. Mechanical parameters adopted in the analytical model to perform numerical analyses.

Parameter	C_1	C_2	C_3	C_4
m_s [kg]	14.2	14.2	7	3.7
k_s [N/m]	150000	3823	80400	600
k_α [Nm]	30.7	30.7	30.7	30.7
c_α [Nms]	57	57	100	57
Mμ [Nm]	7.5	7.5	2	4.5

reduction of normalized acceleration peaks a becomes negative when t equals 2 s and 5 s. Such an apparent contradiction is because the acceleration time histories in ambient vibration tests substantially stop at 1 sec (Fig. 14a). Thus, the results elaborated for t =2 s and t =5 s are shown (Fig. 18) for the sake of completeness, but they do not have physical sense for these ambient vibration tests. Therefore, the method proposed is valid when the time spaces to consider to estimate the acceleration reduction are suitable to the considered ATH. In any case, C_1 exhibits a values in line with the other configurations for t= 1s, actually providing a more beneficial effect with respect to its similar unbraced configuration C_2.

Anyway, the reduction of acceleration demand for all the configurations is between 10% and 40%. The best improvements are registered for C_2 and C_3, which have average values of normalized stiffness $k_s/k_{s,MT}$ equal to about 7 and 140, respectively.

5. Conclusions

This paper analyzed the experimental results of 96 dynamic tests on four configurations of steel superstructures isolated with an innovative base dissipator called Mini Tribological ROCKing Seismic Isolation Device (miniTROCKSISD or MT). Tests on single components that constitute the viscous-elastic dampers are performed to identify their stiffness and damping properties, besides a test for measuring the frictional moment developed at the interface between concave and convex cylindrical surfaces. Afterwards, ambient vibrations and impulsive tests were performed on four specimens that are representative of possible traditional steel structures characterized by different mass and flexibility. They allowed calculating the dynamic properties of the isolated structures (tested with and without MT), highlighting reductions of dominant eigenfrequency from 8% to 15%. The larger reduction was obtained for the multi-story structure, with an experimental reduction of acceleration demand by 30%. Although the reduction of eigenfrequency was not so relevant, the reduction of relative displacement demand was remarkable, between 46% and 56% for the SDOF oscillator and the braced frame structure, respectively. This aspect is of paramount importance since the stresses on the isolated superstructure are strongly reduced.

Moreover, a specific MATLAB code was used to predict the dynamic performances of such a device by comparing experimental and numerical results. The equations of motion of 2DOF and 5DOF systems were written to model the dynamic response of the isolated superstructures. The numerical results were shown to be in very good agreement with experimental tests both in terms of modal properties and displacements. A method to assess the reduction of acceleration demands from impulsive tests was presented, showing a decrease ranging from 10% to 40% depending on the considered time check range. The superstructures, although very different in terms of normalized stiffness, showed a similar reduction of eigenfrequency and a similar reduction of acceleration demand from 10% to 20%, considering as reliable time check range of 1 second. This aspect was shown to be interesting, since, although the normalized stiffness of the superstructures spanned from 1 to 250, a similar improvement was obtained. This issue will be further investigated in the experimental tests on the full-scale specimens (Big TROCKSISD).

ORCID

L. Giresini ⬤ http://orcid.org/0000-0001-6913-7468
F. Laccone ⬤ http://orcid.org/0000-0002-3787-7215

Data availability statement

The data that support the findings of this study are available from the corresponding author, L.G., upon reasonable request.

References

Alecci, V., and M. De Stefano. 2018. Building irregularity issues and architectural design in seismic areas. *Frattura Ed Integrità Strutturale* 13 (47): 161–68. doi: 10.3221/IGF-ESIS.47.13.

Baggio, S., L. Berto, T. Favaretto, A. Saetta, and R. Vitaliani. 2015. Seismic isolation technique of marble sculptures at the accademia gallery in Florence: Numerical calibration and simulation modelling. *Bulletin of Earthquake Engineering* 13 (9): 2719–44. doi: 10.1007/s10518-015-9741-2.

Berto, L., I. Rocca, and A. Saetta. 2018. Vulnerability assessment methods for rocking and overturning of free standing elements. *Soil Dynamics and Earthquake Engineering* 110: 121–36. doi: 10.1016/j.soildyn.2018.02.010.

Borri, A., and A. Grazini. 2006. Diagnostic analysis of the lesions and stability of Michelangelo's David. *Journal of Cultural Heritage* 7 (4): 273–85. doi: 10.1016/j.culher.2006.06.004.

Caliò, I., and M. Marletta. 2003. Passive control of the seismic rocking response of art objects. *Engineering Structures* 25 (8): 1009–18. doi: 10.1016/S0141-0296(03)00045-2.

Casapulla, C. 2015. On the resonance conditions of rigid rocking blocks. *International Journal of Engineering and Technology* 7 (2): 760–71.

Casapulla, C., L. Giresini, L. U. Argiento, and A. Maione. 2019. Nonlinear static and dynamic analysis of rocking masonry corners using rigid macro-block modeling. *International Journal of Structural Stability and Dynamics* 19 (11): 1950137. doi: 10.1142/S0219455419501372.

Casapulla, C., and A. Maione. 2017. Critical response of free-standing rocking blocks to the intense phase of an earthquake. *International Review of Civil Engineering* **8** (1).

Casapulla, C., A. Maione, L. U. Argiento, and E. Speranza. 2018. Corner failure in masonry buildings: An updated macro-modeling approach with frictional resistances. *European Journal of Mechanics - A/Solids* 70: 213–25. doi: 10.1016/j.euromechsol.2018.03.003.

Castaldo, P., and G. Alfano. 2020. Seismic reliability-based design of hardening and softening structures isolated by double concave sliding devices. *Soil Dynamics and Earthquake Engineering* 129: 105930. doi: 10.1016/j.soildyn.2019.105930.

De Canio, G. Marble devices for the Base isolation of the two Bronzes of Riace: A proposal for the David of Michelangelo. *15th World Conference on Earthquake Engineering*, Lisbon, 24th-28th September 2012: 2012.

De Falco, A., L. Giresini, and M. Sassu. 2013. {T}emporary preventive seismic reinforcements on historic churches: Numerical modeling of {S}an {F}rediano in {P}isa. *Applied Mechanics and Materials* 351–352: 1393–96.

Fadi, F., and M. C. Constantinou. 2010. Evaluation of simplified methods of analysis for structures with triple friction pendulum isolators. *Earthquake Engineering & Structural Dynamics* 39 (1): 5–22. doi: 10.1002/eqe.930.

Fenz, D. M., and M. C. Constantinou. 2006. Behaviour of the double concave Friction Pendulum bearing. *Earthquake Engineering & Structural Dynamics* 35 (11): 1403–24. doi: 10.1002/eqe.589.

Froli, M., L. Giresini, and F. Laccone. 2019a. Dynamics of a new seismic isolation device based on tribological smooth rocking (TROCKSISD). *Engineering Structures* 193: 154–69. doi: 10.1016/j.engstruct.2019.05.014.

Froli, M., L. Giresini, and F. Laccone A new seismic isolation device based on tribological smooth rocking (TRockSISD). *7th International Conference on Computational Methods in Structural* Dynamics *and Earthquake* Engineering, *COMPDYN 2019*, Crete, Greece; 24 June 2019 through 26 June 2019: 2019b.

Giresini, L., B. Pantò, S. Caddemi, and I. Caliò Out-of-plane seismic response of masonry façades using discrete macro-element and rigid block models. *COMPDYN 2019 7th ECCOMAS Thematic Conference on Computational Methods in Structural* Dynamics *and* Earthquake Engineering, Crete, Greece; 24th-26th June 2019a: 2019.

Giresini, L., M. Sassu, and L. Sorrentino. 2018. In situ free-vibration tests on unrestrained and restrained rocking masonry walls. *Earthquake Engineering & Structural Dynamics* 47 (15): 3006–25. doi: 10.1002/eqe.3119.

Giresini, L., F. Solarino, O. Paganelli, D. Oliveira, and M. Froli. 2019b. ONE-SIDED rocking analysis of corner mechanisms in masonry structures: Influence of geometry, energy dissipation, boundary conditions. *Soil Dynamics and Earthquake Engineering* 123: 357–70. doi: 10.1016/j.soildyn.2019.05.012.

Giresini, L., F. Taddei, C. Casapulla, and G. Mueller Stochastic assessment of rocking masonry façades under real seismic records. *COMPDYN 2019 7th ECCOMAS Thematic Conference on Computational Methods in Structural* Dynamics *and* Earthquake Engineering, Crete, Greece; 24th-26th June 2019c: 2019.

Lallemant, D., A. Kiremidjian, and H. Burton. 2015. Statistical procedures for developing earthquake damage fragility curves. *Earthquake Engineering & Structural Dynamics* 44 (9): 1373–89. doi: 10.1002/eqe.2522.

Lavan, O., and G. F. Dargush. 2009. Multi-Objective Evolutionary Seismic Design with Passive Energy Dissipation Systems. *Journal of Earthquake Engineering* 13 (6): 758–90. doi: 10.1080/13632460802598545.

MATLAB. 2018. *version 9.4.0.813654 (R2018a)*. Natick, Massachusetts: The MathWorks Inc.

Parulekar, Y. M., and G. R. Reddy. 2009. Passive response control systems for seismic response reduction: A state-of-the-art review. *International Journal of Structural Stability and Dynamics* 09 (01): 151–77.

Soong, T. T., and M. C. Constantinou. 1994. *Passive and active structural vibration control in civil engineering*. New York: Springer.

Sorace, S., and G. Terenzi. 2015. Seismic performance assessment and base-isolated floor protection of statues exhibited in museum halls. *Bulletin of Earthquake Engineering* 13 (6): 1873–92. doi: 10.1007/s10518-014-9680-3.

Stochino, F., A. Attoli, and G. Concu. 2020. Fragility curves for RC structure under blast load considering the influence of seismic demand. *Applied Sciences* 10 (2): 445. doi: 10.3390/app10020445.